Mesoporous NiO crystals with dominantly exposed {110} reactive facets for ultrafast lithium storage

Dawei Su[1], Mike Ford[2] & Guoxiu Wang[1]

[1]Centre for Clean Energy Technology, School of Chemistry and Forensic Science, University of Technology, Sydney, Broadway, Sydney, NSW 2007, Australia, [2]Materials and Technology for Energy Efficiency, School of Physics and Advanced Materials, University of Technology, Sydney, Broadway, Sydney, NSW 2007, Australia.

Faceted crystals with exposed highly reactive planes have attracted intensive investigations for applications such as hydrogen production, enhanced catalytic activity, and electrochemical energy storage and conversion. Herein, we report the synthesis of mesoporous NiO crystals with dominantly exposed {110} reactive facets by the thermal conversion of hexagonal $Ni(OH)_2$ nanoplatelets. When applied as anode materials in lithium-ion batteries, mesoporous NiO crystals exhibit a high reversible lithium storage capacity of 700 mAh g^{-1} at 1 C rate in 100 cycles and an excellent cyclability. In particular, the dominantly exposed {110} reactive facets and mesoporous nanostructure of NiO crystals lead to ultrafast lithium storage, which mimics the high power delivery of supercapacitors.

Faceted crystals with exposed highly reactive crystal plane have great potentials for many applications such as photocatalytic water splitting, new catalysts, and electrochemical energy conversion. However, highly reactive facets usually have high surface energy, and are therefore difficult to synthesise in the equilibrium state. A breakthrough in the synthesis of TiO_2 crystals with 46% high energy {001} facets has recently been achieved by Lu's group[1], which demonstrated excellent photocatalytic activities[2]. Further improvements have also been reported increasing the percentage of the {001} reactive facets of TiO_2 crystals up to 100%[3]. Following studies on TiO_2 facet crystals, Co_3O_4 crystals with exposed high energy planes ({110} and {112}) were also successfully synthesized and applied as catalysts for low temperature oxidation of CO and trace ethylene, and methane combustion[4,5].

Lithium ion batteries are regarded as the choice of power source for vehicle electrification. However, energy and power densities of current generation lithium ion batteries are limited by electrode material. Transition metal oxides have been proposed as high capacity anode materials based on a "conversion" reaction, which is different from the classical insertion/de-insertion[6]. The theoretical capacity of NiO anode is 718 mAh g^{-1}, based on the conversion reaction: $NiO + 2Li^+ + 2e^- \leftrightarrow Li_2O + Ni$. This is almost double the capacity of the graphite anode. NiO is highly favoured as anode materials because of its low cost, low toxicity, and superior safety, compared with other transition metal oxides. Moreover, the density of NiO is 6.67 g cm^{-3}, resulting in high volumetric energy density (about 5.8 times over graphite)[7]. However, the rate performance and cyclability of NiO anode are poor, owing to slow kinetics of the conversion reaction and large volume change of NiO electrode (95.69%) (Table S1, Supplementary Information (SI)). To circumvent these disadvantages, many approaches have been investigated, including the use of carbon materials as a conductive matrix, synthesis of nanostructured nickel oxides (nanocone[8], nanotubes[9], nanofilm[10], and nanowires[11] etc.), and preparation of nickel oxide with porous architecture[11–15]. So far, it has achieved 1031 mAh g^{-1} at 0.1 C (1C = 718 mA g^{-1}) rate[16], 550 mAh g^{-1} at 0.7 C rate[17], 400 mAh g^{-1} at 2 C rate[18], 375 mAh g^{-1} at 10 C rate[19] capacities. It still remains a challenge to attain high rate performance for NiO anode.

Recently, anatase (TiO_2) nanosheets with nearly 100% exposed {001} facets have exhibited a property of fast lithium diffusion in lithium ion cells, but with a low specific capacity less than 200 mAh g^{-1}[3]. It was also reported that the Co_3O_4 nanomesh with exposed {112} high energy facets delivered a good rate capacity above 380 mAh g^{-1} at a discharge rate of 1000 mA g^{-1}[20].

Herein, we report the facile synthesis of mesoporous NiO single crystals with dominantly exposed {110} reactive planes. When applied as anode materials in lithium ion cells, mesoporous NiO crystals exhibited a high

and stable average lithium storage capacity of 700 mAh g^{-1} at 1 C rate and an outstanding capability for ultrafast reversible lithium storage, mimicking supercapacitors.

Results

Characterization of Ni(OH)$_2$ crystals and mesoporous faceted NiO crystals. In the first step of the preparation, faceted Ni(OH)$_2$ crystals were synthesised by a hydrothermal method using SO$_4^{2-}$ ions as the morphology directing agent. Figure 1 shows the field emission scanning electron microscope (FESEM) images, transmission electron microscope (TEM) image and selected area electron diffraction pattern (SAED) of Ni(OH)$_2$ precursor crystals. The hydrothermal product consists of single crystals with a size in the range of 200–400 nm (Fig. 1a). As shown in Figure 1b, the as-obtained Ni(OH)$_2$ crystals have well-defined facets with a truncated symmetric hexagonal pyramid shape. Figure 1c shows a side view of a Ni(OH)$_2$ crystal, from which the thickness can be determined to be about 80 nm. A free-standing Ni(OH)$_2$ crystal is thin enough to be transparent under the electron beam (TEM image of Fig. 1d). The SAED pattern (the inset of Fig. 1d) shows perfect rhombus diffraction spots along the [111] zone axis, indicating the single crystalline feature of Ni(OH)$_2$ crystals. The (110), (101), (011), and (211) atomic planes can be fully indexed. This confirms that the faceted Ni(OH)$_2$ single crystal has the dominantly exposed planes of {111}, which is the only crystal plane normal to all the above indexed crystal planes. The X-ray diffraction pattern (XRD) also confirmed the pure hexagonal phase of Ni(OH)$_2$ crystals with the space group of P$\bar{3}$m1 (Fig. S1, Supplementary Information, SI).

According to the symmetries of Ni(OH)$_2$, the two hexagonal surfaces are the {111} facets and the six isosceles trapezoidal surfaces are the {110}, {011}, and {101} facets. The ratio of the dominantly exposed {111} facets to the total surfaces were estimated to be 95.64% (see the calculation in Supplementary and Fig. S2, SI).

Figure 2a and b show the FESEM images of NiO faceted crystals, which reveal that the hexagonal platelet shape of precursor Ni(OH)$_2$ crystals has been preserved after sintering. X-ray diffraction was performed to determine the phase of NiO crystals (Fig. 2c), in which all diffraction peaks can be indexed to the cubic symmetry with the space group of Fm$\bar{3}$m. The BET surface area and porosity of NiO crystals were investigated by nitrogen adsorption/desorption isotherms at 77 K. As shown in Figure 2d, the hysteresis feature of the NiO crystals can be classified as the typical-IV isotherm with an H$_1$-type loop, reflecting the mesoporous nature of the NiO crystals. The pore size distribution curve is shown as the inset of Figure 2d, which exhibits a monomodal pore size distribution with a mean pore size of 9.32 nm (calculated by the Barrett-Joyner-Halenda (BJH) method). The specific BET surface area and total pore volume were determined to be 197.5 m^2 g^{-1} and 1.22 cm^3 g^{-1}, respectively.

The morphology and crystal structure of the mesoporous faceted NiO crystals were further characterised by TEM and HRTEM. It is evidenced from the bright-field TEM images of mesoporous NiO crystals in Figure 3a and b, from which we can see that NiO crystals maintain the faceted nanoplatelet shape with a porous architecture. Figure S3 (Supplementary) also shows other NiO faceted crystals, which have a hexagonal nanoplate shape. The insets in Figure 3a and b present the corresponding SAED patterns along the [110] zone
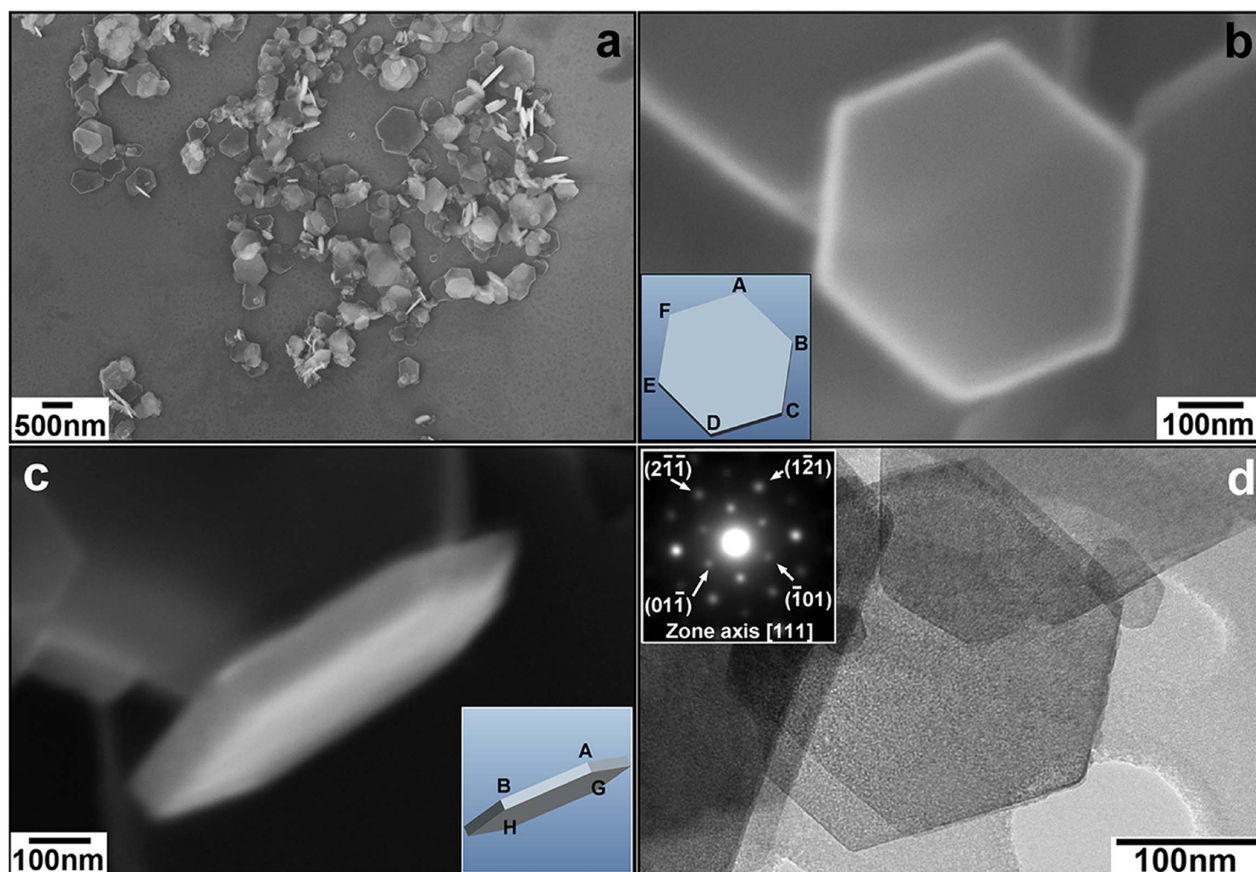
Figure 1 | Ni(OH)$_2$ crystals. (a) A low magnification FESEM image of Ni(OH)$_2$ faceted crystals. (b) A high magnification FESEM image of Ni(OH)$_2$ faceted crystals, showing hexagonal platelet shape. (c) The side view of a Ni(OH)$_2$ crystal, from which the thickness can be determined. (d) TEM image of faceted Ni(OH)$_2$ crystal. The insets of (b) and (c) are the corresponding simulated model of the faceted crystals. The inset in (d) shows the SAED pattern along the [111] zone axis.
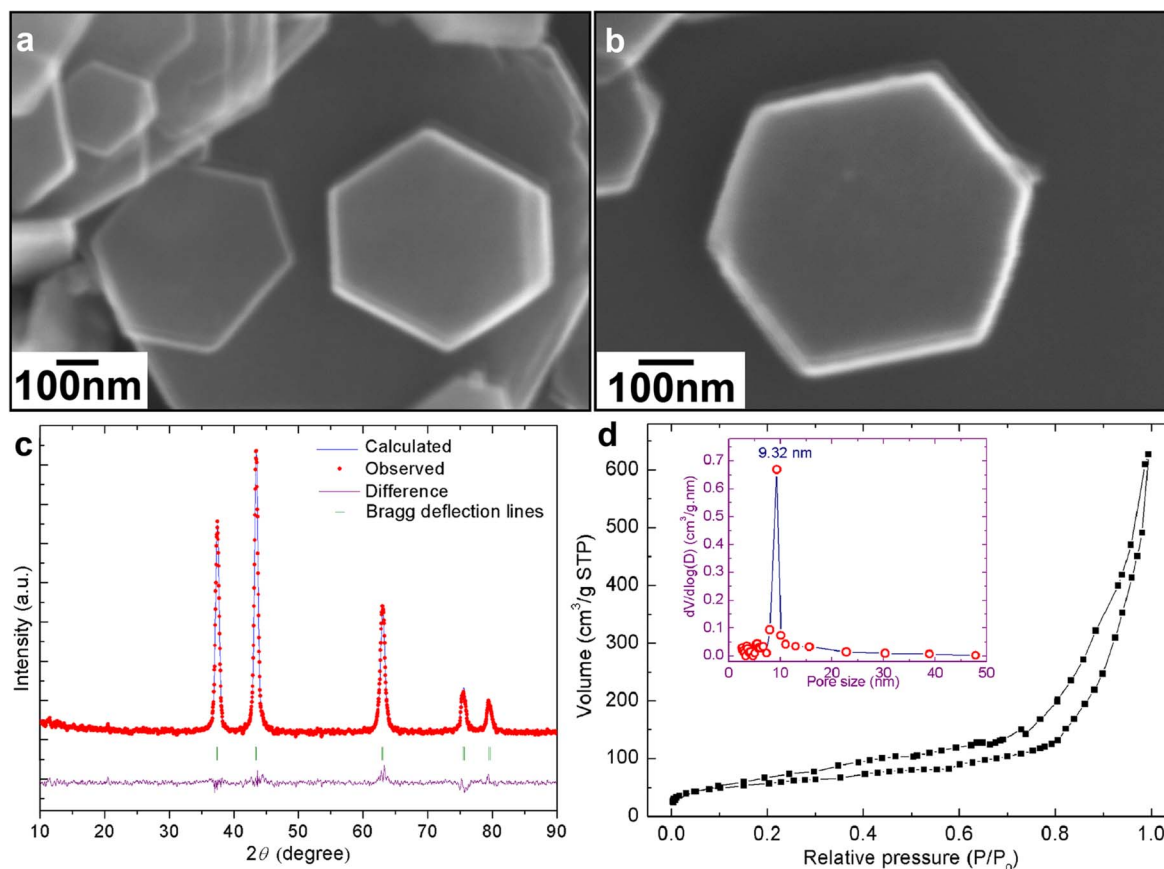
Figure 2 | Morphology and Phase analysis of NiO mesoporous crystals. (a) and (b) FESEM images of NiO faceted crystals. (c) Rietveld refinement pattern of X-ray diffraction data of NiO crystals, the observed and calculated intensity are represented by red solid circle and blue solid line, respectively. The bottom purple line shows the fitting residual difference. Bragg positions are represented as light green tick. (d) N$_2$ sorption isotherms of mesoporous faceted NiO crystals. The inset shows the pore size distributions.
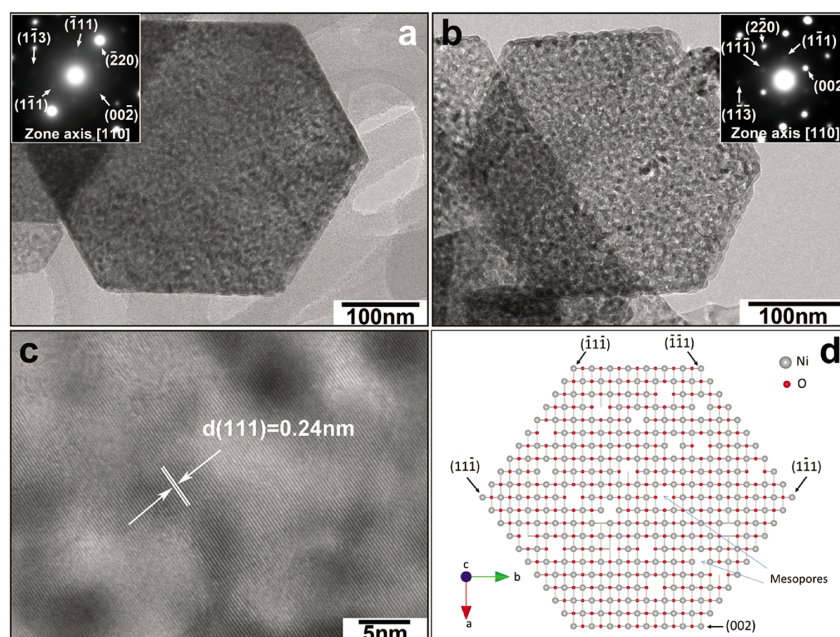
Figure 3 | Structure analysis of NiO mesoporous crystals. (a) and (b) are TEM images of individual NiO faceted crystals. (c) Lattice resolved HRTEM image of NiO crystals. (d) Schematic diagram of crystal structure of as-prepared NiO faceted crystals. Insets in (a) and (b) are SAED along the [110] zone axis.

axis. The dot SAED patterns imply the single crystalline nature of the mesoporous NiO crystals, from which the (111), (002), and (220) planes can be indexed. The normal direction to the dominantly exposed crystal planes (hexagon surface) is the [110] axis, which is coincident with the direction of the electron beam. Figure 3c shows a lattice resolved HRTEM image of a NiO crystal, in which the lattice can be determined to be the (111) crystal plane with a d spacing of 0.24 nm. As illustrated in Figure 3d, the mesoporous NiO crystals have the dominantly exposed {110} planes on both hexagon surfaces together with {002} and {111} facet planes, forming a close-packed hexagonal nanoplatelet. Although there are dense mesopores dispersing in each NiO nanoplatelet, the {110} crystal planes still occupy about 66% of the total surface area after counting the total pore area (see the calculation in the Supplementary Information).

Crystal growth mechanism. In the alkaline solution under hydrothermal condition, Ni^{2+} ions react with OH^- to form $Ni(OH)_2$ crystals. The previous study has shown that sulphate ions (SO_4^{2-}) are most strongly adsorbed to the surfaces perpendicular to the c-axis of the hexagonal crystal system through bridging-bidentate adsorption, leading to retarded growth in the direction along the c-axis[21]. As a result, the faceted hexagon nanoplate shape was formed. $Ni(OH)_2$ decomposed to NiO crystals in the sintering process, during which the mesoporous structure was generated simultaneously. The crystal growth and conversion processes are illustrated in Scheme S1 (SI). NiO crystals preserved the single crystalline feature and hexagonal shape of the precursor $Ni(OH)_2$ nanoplatelets, which could be attributed to the low crystal mismatch between $Ni(OH)_2$ and NiO crystals[20]. Because the {111} crystal planes of $Ni(OH)_2$ and {110} crystal planes of NiO have low crystal mismatch as illustrated in the Scheme S2 (SI). For example, the $(1\bar{1}0)$ lattice planes of $Ni(OH)_2$ crystals has a d-spacing of 0.29 nm, which is very close to d-spacing of the $(\bar{1}11)$ planes of NiO crystals (0.24 nm). The control of the crystal mismatch within a low range is highly favourable for monocrystallization[22]. Therefore, the monocrystallization and conversion from $Ni(OH)_2$ to NiO can be considered as a thermodynamically favoured recrystallization process, during which the single crystalline was maintained throughout the whole transformation. The partial collapse of the porous structure upon template-removal or thermal annealing is always inevitable in the preparation of amorphous or polycrystalline mesoporous structures through the conventional template route[23]. The reported solid-state crystal reconstruction is a facile approach to obtain uniform mesoporous structures with 3D single crystal framework.
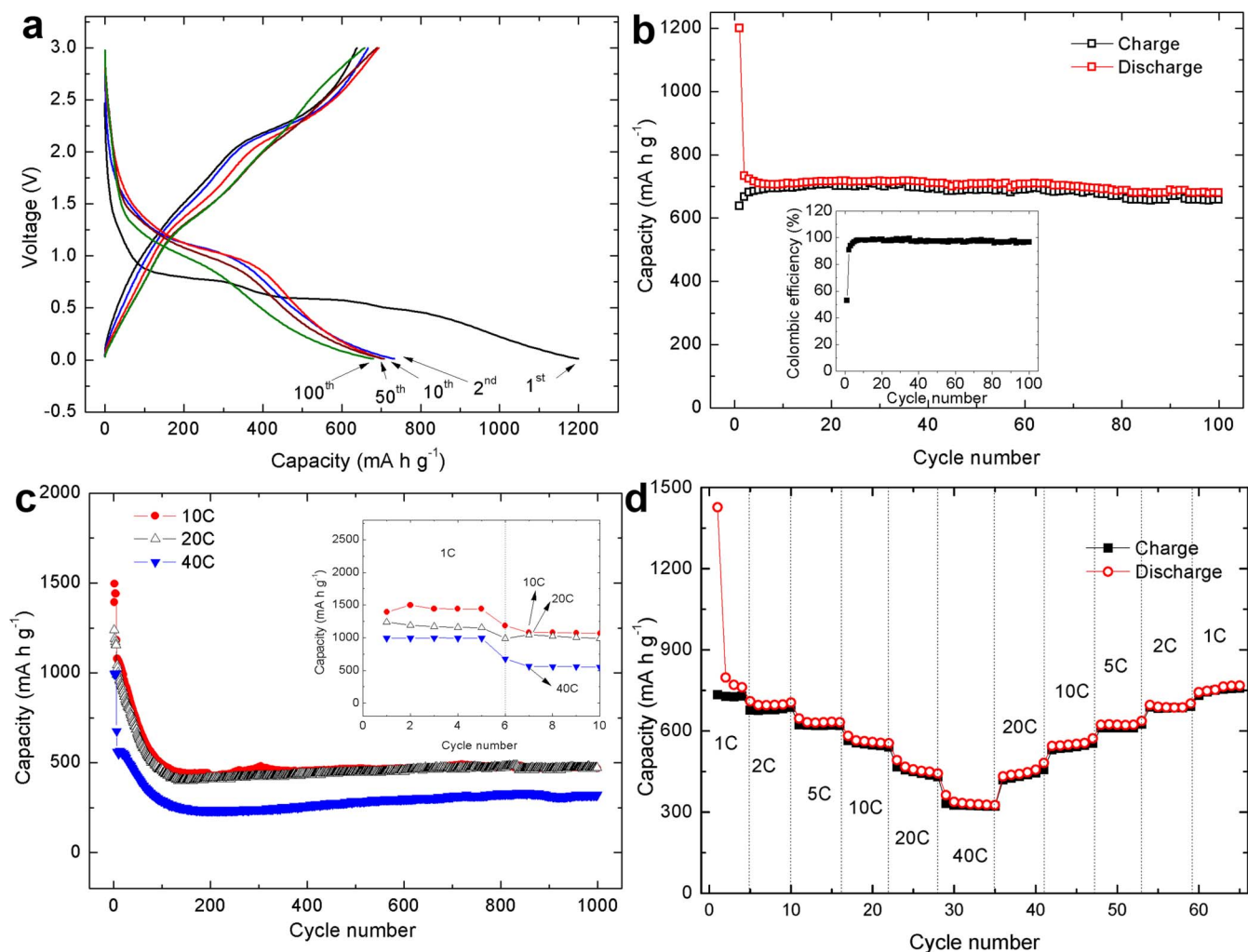
Electrochemical properties of mesoporous NiO crystals for lithium storage in lithium ion batteries. The electrochemical properties of mesoporous NiO crystals were tested by cyclic voltammetry (CV) and galvanostatical charge and discharge cycling. The CV curves were shown in Figure S4 (Supplementary), reflecting reversible lithium storage of NiO crystals. Figure 4a shows the charge and discharge profiles in the 1st, 2nd, 10th, 50th and 100th cycles at 1 C rate. In the first cycle, the electrode delivered a capacity of 1200 mAh g^{-1}, in which partial capacity could be consumed for the formation of solid electrolyte interphase layer (SEI)[24,25]. From the second cycle, the electrode maintained high reversibility. The cycling performance of mesoporous NiO crystal at 1 C is presented in Figure 4b. After 100 cycles, the electrode still retained a capacity of 682 mAh g^{-1}. The corresponding Coulombic efficiency is shown as the inset in Figure 4b. The mesoporous NiO crystal electrodes were cycled at high rates of 10 C, 20 C, and 40 C for 1000 cycles. The electrodes exhibited almost the same capacity and cycling performance at 10 C and 20 C. After 1000 cycles, mesoporous NiO crystals retained lithium storage capacity of 468 mAh g^{-1} at 10 C and 20 C rate, and 322 mAh g^{-1} at 40 C rate, respectively. This performance is much better than that of carbon based anode materials[26,27]. We also tested the cycling performance at varied

current rates: 1 C, 2 C, 5 C, 10 C, 20 C, and 40 C. The results are presented in Figure 4d. It should be noticed that as long as the current rate reversed back low current rate, the cell capacity recovered to the original values, indicating that the integrity of mesoporous NiO crystals has been preserved even after high rate cycling. This implies that mesoporous NiO crystals are tolerant to varied charge and discharge currents, which is preferred for high power applications. Mesoporous NiO crystals exhibited a much higher capacity than the previously reported NiO anode materials[7,12,28], mesoporous NiO synthesized by the hard template method[15], and NiO/graphene hybrid anode materials[29,30].

Discussion

The refined crystal structure and relaxed side views of $Ni(OH)_2$ and NiO are shown in Figure S5 and Figure S6 (Supplementary), respectively. $Ni(OH)_2$ has a tabular crystal structure, in which the NiO_6 octahedrons are compressed parallel to the threefold axis, inducing an enlargement of the distance between the oxygen atoms at positions (1/3, 2/3, z) and (2/3, 1/3, −z). The structure of NiO is commonly known as the rock salt structure in which octahedral Ni (II) and O^{2-} occupy the 4 a and 4 b sites, respectively. The calculated surface energies for $Ni(OH)_2$ and NiO crystals are listed in table S2 and S3, respectively (Supplementary). The (111) plane of $Ni(OH)_2$ crystal has the lowest energy of 0.952 J m^{-2}, suggesting it is the most stable. The other crystal planes have higher surface energies, indicating these are meta-stable surfaces. Thus, it is possible to grow $Ni(OH)_2$ crystals with a high percentage of exposed {111} facets. This theoretical predication was confirmed in this investigation. The most stable crystal plane for NiO crystal is the {100} facet with the lowest surface energy of 0.958 J m^{-2}. The {113} plane has the second lowest surface energy (1.264 J m^{-2}). The {110} and {101} planes have relatively high value larger than 1.47 J m^{-2}. Therefore, it is not favourable to obtain highly exposed {110} facets for NiO crystals under the equilibrium condition. Since the $Ni(OH)_2$ crystals have a nanoplatelet shape, in which the two basal planes ({111} facets) are dominantly exposed crystal planes. After sintering, the nanoplatelet shape was preserved for NiO crystals, in which the two basal planes indexed as the {110} facets, are still dominantly exposed planes. Generally, high-energy surfaces have a large density of low-coordinated atoms situated on steps and kinks, with high reactivity[31]. This favours fast ion transfer between the surface and the interior[32,33]. Because the {110} facets have relatively high surface energy, the {110} crystal planes provide reactive sites for reaction with lithium ions, which can facilitate fast conversion reaction towards lithium during the charge and discharge process. On the other hand, the mesoporous architecture contributes to the excellent electrochemical performance of NiO crystals. In lithium-ion cells, liquid electrolyte can flood into mesopores, inducing high surface area contact with active NiO crystals. Thin nanoplate and mesoporous structure provide a short path for lithium transport and high surface area for interfacial lithium storage[25,34].

In order to investigate the lithium-driven structural and morphological changes during the charge and discharge processes, we performed *ex-situ* TEM and SAED analysis on mesoporous facet NiO crystals at the fully discharged (reduced) and charged (oxidized) states in the first cycle and the 100th cycle at 1 C rate. The results are shown in Figure 5. At the fully discharged state in the first cycle, the crystal shape was preserved and the surface of the crystal became rough as shown in the bright-field TEM image (Fig. 5a). NiO was reduced to metallic Ni and dispersed in the lithia (Li_2O) matrix[6]. The corresponding SAED pattern presents the (200), (220) and (311) diffraction rings of Li_2O (Fig. 5b). HRTEM (Fig. 5c) reveals the pseudo-amorphous characteristic, suggesting the formation of the solid electrolyte interphase layer. After being fully charged in the first cycle, the NiO crystals recovered to the pristine state. As shown in Figure 5d, individual crystals have a clear hexagon appearance

Figure 4 | Electrochemical characterizations. (a) Discharge and charge profiles of mesoporous NiO crystals at 1 C current rates. (b) Cycling performance of mesoporous NiO crystals at 1 C current rates. The inset of (b) shows the Coulombic efficiency. (c) Discharge capacity vs. cycle number of mesoporous NiO crystals at high current rates of 10 C, 20 C, and 40 C. The inset shows discharge capacity in the initial 10 cycles. (d) The rate performance of mesoporous NiO crystals at varied current rates.

with smooth surface. When taking SAED from an individual crystal, spot SAED patterns were obtained (Fig. 5e). The SAED pattern can be well indexed to NiO crystal along the [110] zone axis. This unambiguously confirmed the recovery of the single crystalline feature at the fully charge state for mesoporous NiO crystals in the first cycle. A lattice resolved HRTEM image (Fig. 5f) shows the $(\bar{1}1\bar{1})$ and $(\bar{1}11)$ crystal planes with a d-spacing of 2.5 Å and 109° angle. The fast Fourier transform (FFT) spot pattern (the inset in Fig. 5f) further confirms the single crystalline feature. Mesoporous structure can also be clearly observed in Figure 5f. Therefore, mesoporous faceted NiO crystals can fully recover to their original states after the first cycle.

To further illustrate the outstanding cycle performance of facet NiO crystals, we conducted post-morten TEM analysis on the electrode at the discharged and charged states in the 100th cycle. When the electrode was fully discharged after 100 cycles, the crystals still maintained the original appearance (the bright-field TEM image, Fig. 5g), which is similar to that after the initial cycle. The SAED ring pattern (Fig. 5h) can be indexed to Li_2O. Figure 5i shows the HRTEM image of the NiO crystal at the discharged state in the 100th cycle, from which the mesoporous architecture can be easily distinguished. Figure 5j shows the bright-field TEM image of NiO crystals at the fully charged state in the 100th cycle. The hexagonal nanoplate shape was restored even after 100 cycles. The SAED spot pattern

(Fig. 5k) taken from individual crystal can be fully indexed along the [110] zone axis of cubic NiO. This suggests the recovery of single crystalline NiO after long time cycling. The corresponding HRTEM image is presented in Figure 5l, from which the (111) crystal planes of NiO with a d-spacing of 0.24 nm can be indexed. The regular mesopores are also visible from the HRTEM image. The FFT pattern shows the spot feature, further illustrating the single crystalline of NiO crystals. We also performed the ex-situ observation of mesoporous facet NiO crystals after 100 cycles at 0.5 C and after 1000 cycles at 10, and 40 C current rates by FESEM. Figure S7 shows the FESEM images of the individual mesoporous NiO crystals at the fully charged states. All crystals were restored to faceted crystal shape with good crystalinity even cycled at high current rate of 40 C.

Recently, J.-M tarascon *et al.* have identified a special mechanism for reversible lithium storage in mesoporous metal oxides (MO), which differs from bulk materials[35]. They found that mesoporous MO reacts with Li through a conversion reaction, leading to the formation of large metallic M nanoparticles (10 nm) upon discharge. These nanoparticles are embedded into a Li_2O matrix together with a copious amount of polymeric materials coming from electrolyte degradation, which surround the particles and fill the pores. During the following charge, re-oxidation of the nanoparticles occurs with the formation of MO. The main difference, when

5
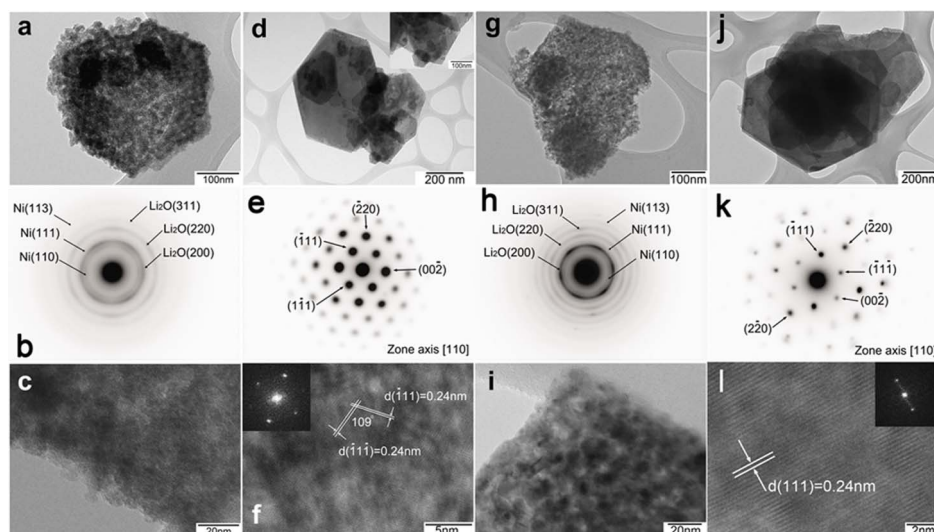
Figure 5 | Structural and morphological changes of mesoporous NiO facet crystals during the charge and discharge processes. TEM images and SAED patterns of NiO electrodes taken from fully discharged states (a)–(c) and fully charged states (d)–(f) in the first cycle, fully discharged (g)–(i) and fully charged (j)–(l) states after 100 cycles. (a), (d), (g), and (j) show bright-field TEM images of individual NiO crystals at different stages of the reduction and oxidation processes. (b), (e), (h), and (k) are the corresponding SAED patterns. (c), (f), (i), and (l) are the lattice resolved TEM images at various stages of the reduction and oxidation processes. The inset in (d) is the magnified TEM image of a NiO facet crystal. The insets in (f) and (l) are the corresponding FFT images.

compared to bulk MO electrodes, is the preservation of the polymeric layer at the end of the charge. Therefore, the origin of this difference lies in the material mesoporosity, via capillary effects. Our mesoporous NiO crystals match this newly discovered mechanism. The mesoporous structure has been preserved during discharge and charge processes, owing to the formation of polymeric SEI layer. Mesoporous NiO crystals with exposed {110} facets were restored during charging, which has been confirmed by *ex-situ* TEM analysis.

In summary, mesoporous faceted NiO crystals were synthesised by a hydrothermal method combined with annealing treatment. TEM analysis confirmed that NiO crystals had dominantly {110} exposed crystal planes and mesoporous architecture. When applied as anode materials in lithium-ion cells, mesoporous faceted NiO crystals delivered a high reversible lithium storage capacity of around 700 mAh g^{-1} in 100 cycles with high Coulombic efficiency at 1 C current rate. The materials also demonstrated an outstanding high rate performance, which mimics supercapacitors for high power delivery. *Ex-situ* TEM characterisation clearly illustrated that the mesoporous and faceted crystal structure had been retained after long term discharge/charge cycling even at high current rates. The mesoporous and faceted crystal architecture may be extended to other electrode materials for energy storage applications with high performance.

Methods

Synthesis of facet Ni(OH)$_2$ crystals and mesoporous faceted NiO crystals. The faceted Ni(OH)$_2$ single crystalline crystals were synthesized by a hydrothermal method. In a typical synthesis process, 0.02 mol NiCl$_2$ (Sigma-Aldrich, ≥ 97%) was dissolved in 10 ml distilled water. Then 10 ml 6 M NaOH (Sigma-Aldrich, ≥ 98%) solution was added under vigorous stirring. After a pink transparent solution formed gradually, 0.6 mmol Na$_2$SO$_4$ (Sigma-Aldrich, ≥ 98%) was added into the solution. The mixture was then transferred into a Teflon-lined autoclave and heated at 170°C for 24 hours in an air-flow electric oven. After cooling to room temperature, the pink product was collected by centrifugation and washed thoroughly with distilled water several times. The Ni(OH)$_2$ crystals were obtained after drying for 12 h at 60°C in the vacuum oven. The final mesoporous faceted NiO crystals were prepared by annealing the Ni(OH)$_2$ precursor at 500°C for 5 h.

Structural and physical characterization. The crystal structure and phase of the as-prepared materials were characterized by X-ray diffraction (XRD, Siemens D5000) using a Cu Kα radiation at a scanning step of 0.02°/min. The morphology was analyzed by field emission scanning electron microscopes (FESEM, Zeiss Supra

55VP). The structure details were further characterized by transmission electron microscopy (TEM) and high-resolution transmission electron microscopy (HRTEM, JEOL JEM-2011). Selected area electron diffraction (SAED) patterns were recorded by a Gatan CCD camera in a digital format.

Electrochemical testing. The electrodes were prepared by dispersing the as-prepared NiO crystals (70 wt%), acetylene carbon black (20 wt%), and poly (Vinylidene fluoride) binder (PVDF, 10 wt%) in N-methyl-2-pyrrolidone (NMP) to form a slurry. The resultant slurry was pasted onto copper foil using a doctor blade and dried at 100°C for 12 h under vacuum, followed by pressing at 200 kg cm^{-2}. Electrochemical measurements were carried out using two-electrode coin cells with lithium metal as the counter electrode. The CR2032-type coin cells were assembled in an argon-filled glove box (UniLab, Mbraun, Germany). The electrolyte solution was 1 M LiPF$_6$ dissolved in a mixture of ethylene carbonate (EC) and dimethyl carbonate (DMC) with a volume ratio of 1:1. Cyclic voltammetry (CV) was carried out on a CHI 660C electrochemistry workstation with a scan rate of 0.1 mV s^{-1} from 0.01 to 3.0 V in a two-electrode system. The charge-discharge measurements were performed at ambient temperature at different current densities in the voltage range from 0.01 to 3.0 V. In order to investigate the lithium-driven structural and morphological changes of mesoporous faceted NiO crystals during the lithium insertion and extraction processes, Swagelok-type cells were assembled. The cells were discharged or charged to the required voltages and then opened in the Glove-box. The partially lithiated or de-lithiated materials were removed from the electrodes and washed with dimethyl carbonate (DMC) before being placed onto a copper grid mounted on the TEM sample holder.

Computational methods. The calculations were performed based on the density-functional theory (DFT) +U approach[36] with the ABINIT[37,38]. The exchange-correlation energy function was represented by the local-density approximation (LDA) employing ultra-soft pseudopotential (USPP) formalism[39]. We used an energy cutoff of 350 eV. Monkhorst-Pack k-point sets of 6×6×6 were used. The on-site Coulomb repulsion (Hubbard U) was applied for Ni d states. The effective values for U of 8.0 eV for Ni had been derived by fitting to experimental oxidation enthalpies and it will gave better estimates for band gaps[40]. The maximum self-consistent field convergent tolerance was less than 2×10^{-6} eV atom^{-1}. All calculations were performed in reciprocal space. To predict the morphology and surface energy of Ni(OH)$_2$ and NiO, a set of suitable faces were used. The surface region in our calculation is composed of a finite number of two-dimensional infinite planes formed by cutting the crystal along a particular Miller index (hkl) plane. In each plane, a two-dimensional cell represents every site in the plane. Following the approach of Tasker[41], several of these cells in successive planes comprise the basic repeat unit that contains the composition of the bulk crystal unit cell. The surface energy per unit area, $E_{surface}^{hkl}$, of a particular surface is calculated from the difference between the energy of the surface block, $E_{surface\,block}$, and the energy of the same number of bulk ions, E_{bulk}, per unit area, A (cross-sectional), thus

$$E_{surface}^{hkl} = \frac{E_{surface\,block} - E_{bulk}}{A} \qquad (1)$$

6

For slab model construction, 8 layers were used and the depths of the surface regions were chosen to be large enough to ensure full relaxation of the surface ions and convergence of the surface energy. In each case, surface structures were fully relaxed until the total energy difference was converged within 0.001 eV.

1. Yang, H. G. *et al*. Anatase TiO₂ single crystals with a large percentage of reactive facets. *Nature* **453**, 638–642 (2008).
2. Yang, H. G. *et al*. Solvothermal Synthesis and Photoreactivity of Anatase TiO₂ Nanosheets with Dominant {001} Facets. *Journal of the American Chemical Society* **131**, 4078–4083 (2009).
3. Chen, J. S. *et al*. Constructing Hierarchical Spheres from Large Ultrathin Anatase TiO₂ Nanosheets with Nearly 100% Exposed (001) Facets for Fast Reversible Lithium Storage. *Journal of the American Chemical Society* **132**, 6124–6130 (2010).
4. Xie, X., Li, Y., Liu, Z. Q., Haruta, M. & Shen, W. Low-temperature oxidation of CO catalysed by Co₃O₄ nanorods. *Nature* **458**, 746–749 (2009).
5. Hu, L., Peng, Q. & Li, Y. Selective Synthesis of Co₃O₄ Nanocrystal with Different Shape and Crystal Plane Effect on Catalytic Property for Methane Combustion. *Journal of the American Chemical Society* **130**, 16136–16137 (2008).
6. Poizot, P., Laruelle, S., Grugeon, S., Dupont, L. & Tarascon, J. M. Nano-sized transition-metaloxides as negative-electrode materials for lithium-ion batteries. *Nature* **407**, 496–499 (2000).
7. Li, X. F., Dhanabalan, A. & Wang, C. L. Enhanced electrochemical performance of porous NiO-Ni nanocomposite anode for lithium ion batteries. *Journal of Power Sources* **196**, 9625–9630 (2011).
8. Wang, X. *et al*. NiO nanocone array electrode with high capacity and rate capability for Li-ion batteries. *Journal of Materials Chemistry* **21**, 9988–9990 (2011).
9. Needham, S. A., Wang, G. X. & Liu, H. K. Synthesis of NiO nanotubes for use as negative electrodes in lithium ion batteries. *Journal of Power Sources* **159**, 254–257 (2006).
10. Wu, M. S. & Lin, Y. P. Monodispersed macroporous architecture of nickel-oxide film as an anode material for thin-film lithium-ion batteries. *Electrochimica Acta* **56**, 2068–2073 (2011).
11. Su, D., Kim, H. S., Kim, W. S. & Wang, G. Mesoporous Nickel Oxide Nanowires: Hydrothermal Synthesis, Characterisation and Applications for Lithium-Ion Batteries and Supercapacitors with Superior Performance. *Chemistry-A European Journal* **18**, 8224–8229 (2012).
12. Xia, Y. *et al*. Biotemplated fabrication of hierarchically porous NiO/C composite from lotus pollen grains for lithium-ion batteries. *Journal of Materials Chemistry* **22**, 9209–9215 (2012).
13. Chen, Z. *et al*. Template-directed preparation of two-layer porous NiO film via hydrothermal synthesis for lithium ion batteries. *Materials Research Bulletin* **47**, 1987–1990 (2012).
14. Chen, X., Zhang, N. & Sun, K. Facile ammonia-induced fabrication of nanoporous NiO films with enhanced lithium-storage properties. *Electrochemistry Communications* **20**, 137–140 (2012).
15. Liu, H., Wang, G. X., Liu,J., Qiao, S. Z. & Ahn, H. J. Highly ordered mesoporous NiO anode material for lithium ion batteries with an excellent electrochemical performance. *Journal of Materials Chemistry* **21**, 3046–3052 (2011).
16. Zou, Y. & Wang, Y. NiO nanosheets grown on graphene nanosheets as superior anode materials for Li-ion batteries. *Nanoscale* **3**, 2615–2620 (2011).
17. Huang, X. H., Tu, J. P., Zeng, Z. Y., Xiang, J. Y. & Zhao, X. B. Nickel foam-supported porous NiO/Ag film electrode for lithium-ion batteries. *Journal of the Electrochemical Society* **155**, A438–A441 (2008).
18. Zhong, J. *et al*. Self-assembled sandwich-like NiO film and its application for Li-ion batteries. *Journal of Alloys and Compounds* **509**, 3889–3893 (2011).
19. Wang, X. *et al*. Nanostructured NiO electrode for high rate Li-ion batteries. *Journal of Materials Chemistry* **21**, 3571–3573 (2011).
20. Wang, Y. *et al*. Crystal-match guided formation of single-crystal tricobalt tetraoxygen nanomesh as superior anode for electrochemical energy storage. *Energy & Environmental Science* **4**, 1845–1854 (2011).
21. Zhang, J. H., Liu, H. Y., Zhan, P., Wang, Z. L. & Ming, N. B. Controlling the growth and assembly of silver nanoprisms. *Advanced Functional Materials* **17**, 1558–1566 (2007).
22. Rumplecker, A., Kleitz, F., Salabas, E. L. & Schuth, F. Hard templating pathways for the synthesis of nanostructured porous Co₃O₄. *Chemistry of Materials* **19**, 485–496 (2007).
23. Shaju, K. M., Jiao, F., Debart, A. & Bruce, P. G. Mesoporous and nanowire Co₃O₄ as negative electrodes for rechargeable lithium batteries. *Physical Chemistry Chemical Physics* **9**, 1837–1842 (2007).
24. Balaya, P., Li, H., Kienle, L. & Maier, J. Fully reversible homogeneous and heterogeneous Li storage in RuO₂ with high capacity. *Advanced Functional Materials* **13**, 621–625 (2003).
25. Maier, J. Nanoionics: ion transport and electrochemical storage in confined systems. *Nature Materials* **4**, 805–815 (2005).
26. Wang, G. X., Shen, X. P., Yao, J. & Park, J. Graphene nanosheets for enhanced lithium storage in lithium ion batteries. *Carbon* **47**, 2049–2053 (2009).
27. Fang, B., Kim, M. S., Kim, J. H., Lim, S. & Yu, J. S. Ordered multimodal porous carbon with hierarchical nanostructure for high Li storage capacity and good cycling performance. *Journal of Materials Chemistry* **20**, 10253–10259 (2010).
28. Ni, S. B., Li, T. & Yang, X. L. Fabrication of NiO nanoflakes and its application in lithium ion battery. *Materials Chemistry and Physics* **132**, 1108–1111 (2012).
29. Mai, Y. J. *et al*. NiO-graphene hybrid as an anode material for lithium ion batteries. *Journal of Power Sources* **204**, 155–161 (2012).
30. Huang, Y. *et al*. Self-assembly of ultrathin porous NiO nanosheets/graphene hierarchical structure for high-capacity and high-rate lithium storage. *Journal of Materials Chemistry* **22**, 2844–2847 (2012).
31. Lebedeva, N. P., Koper, M. T. M., Feliu, J. M. & van Santen, R. A. Role of crystalline defects in electrocatalysis: Mechanism and kinetics of CO adlayer oxidation on stepped platinum electrodes. *Journal of Physical Chemistry B* **106**, 12938–12947 (2002).
32. Zhang, D. Q. *et al*. Microwave-Induced Synthesis of Porous Single-Crystal-Like TiO₂ with Excellent Lithium Storage Properties. *Langmuir* **28**, 4543–4547 (2012).
33. Chen, J. S., Liu, H., Qiao, S. Z. & Lou, X. W. Carbon-supported ultra-thin anatase TiO₂ nanosheets for fast reversible lithium storage. *Journal of Materials Chemistry* **21**, 5687–5692 (2011).
34. Hu, Y. S., Kienle, L., Guo, Y. G. & Maier, J. High lithium electroactivity of nanometer-sized rutile TiO₂. *Advanced Materials* **18**, 1421–1426 (2006).
35. Dupont, L. *et al*. Mesoporous Cr₂O₃ as negative electrode in lithium batteries: TEM study of the texture effect on the polymeric layer formation. *Journal of Power Sources* **175**, 502–509 (2008).
36. Amadon, B., Jollet, F. & Torrent, M. gamma and beta cerium: LDA+U calculations of ground-state parameters. *Physical Review B* **77**, 155104(155101)–155104(155110) (2008).
37. Gonze, X. *et al*. ABINIT: First-principles approach to material and nanosystem properties. *Comput Phys Commun* **180**, 2582–2615 (2009).
38. Gonze, X. *et al*. A brief introduction to the ABINIT software package. *Z Kristallogr* **220**, 558–562 (2005).
39. Perdew, J. P. & Wang, Y. Accurate and Simple Analytic Representation of the Electron-Gas Correlation-Energy. *Physical Review B* **45**, 13244–13249 (1992).
40. Vanderbilt, D. Soft Self-Consistent Pseudopotentials in a Generalized Eigenvalue Formalism. *Physical Review B* **41**, 7892–7895 (1990).
41. Tasker, P. W. Stability of Ionic-Crystal Surfaces. *J Phys C Solid State* **12**, 4977–4984 (1979).

Acknowledgment

Author contributions

D.-W. S. performed the theoretical calculations and modelling, experiments and testing. M.F. discussed the theoretical calculations. G.-X. W. designed the experiments, discussed the results and co-wrote the manuscript.

Additional information

Supplementary information accompanies this paper at http://www.nature.com/scientificreports

How to cite this article: Su, D., Ford, M. & Wang, G. Mesoporous NiO crystals with dominantly exposed {110} reactive facets for ultrafast lithium storage. *Sci. Rep.* **2**, 924; DOI:10.1038/srep00924 (2012).